Fourier transform interferometer alignment method

Kenneth A. Goldberg, Patrick Naulleau, and Jeffrey Bokor

A rapid and convenient method has been developed to facilitate the alignment of the image-plane components of point-diffraction interferometers, including the phase-shifting point-diffraction interferometer. In real time, the Fourier transform of the detected image is used to calculate a pseudoimage of the electric field in the image plane of the test optic where the critical alignment of various optical components is performed. Reconstruction of the pseudoimage is similar to off-axis, Fourier transform holography. Intermediate steps in the alignment procedure are described. Fine alignment is aided by the introduction and optimization of a global-contrast parameter that is easily calculated from the Fourier transform. Additional applications include the alignment of image-plane apertures in general optical systems, the rapid identification of patterned image-plane alignment marks, and the probing of important image-plane field properties. © 2002 Optical Society of America

OCIS codes: 070.2580, 090.1760, 120.2880, 120.3180, 220.4840.

1. Introduction

Interferometers that generate a reference wave front by means of diffraction from a small object or aperture are called point-diffraction interferometers (PDI). These interferometers typically offer the advantages of a common-path design and minimal coherence-length requirements while obviating reference surfaces. Many PDI configurations have been described,[1–5] including some that enable phase shifting.[6,7] One recently invented PDI, described by Medecki *et al*.[8] incorporates a beam splitter that spatially separates the test and reference beams in the image plane, enabling phase-shifting techniques to be introduced. This interferometer, named the phase-shifting PDI (PS/PDI), has generated interest because of its demonstrated capability for high accuracy optical system testing[9] and its suitability for the measurement of diffraction-limited, short-wavelength optical systems in which subangstrom rms accuracy is required.

In the PS/PDI two spherical-wave reference beams are generated by pinhole diffraction in the object and image planes of an optical system under test. The

design of the PS/PDI is shown in Fig. 1. A pinhole located in the object plane spatially filters the illumination source to produce a spatially coherent illuminating beam. A coarse, grating beam splitter placed before the image plane, on either the object or the image side of the test optic, generates multiple, focused coherent beams that are spatially separated in the image plane. One beam containing the aberrations of the optical system is allowed to pass through a large window in an opaque membrane located in the image plane; this becomes the test beam. A second beam is brought to focus on a reference pinhole smaller than the diffraction-limited resolution of the test optic, where it is spatially filtered to become a spherical reference beam that diffracts to overlap the numerical aperture (NA) of measurement. The test and reference beams propagate from the image plane to a detector where their interference pattern is recorded. With or without reimaging optics, the detector is typically positioned to capture the full NA of the test optic. A controllable phase shift between the test and the reference beams is achieved by a simple lateral translation of the grating beam splitter.

Using pinholes smaller than the diffraction-limited resolution of the optical system is the key to the reference-wave accuracy of the interferometer. With its common-path design and limited number of components, the PS/PDI is somewhat easy to implement and use; yet in practice, the process of aligning the pinhole in the image plane can be very challenging.

The PS/PDI has been successfully used in the measurement of multilayer-coated, all-reflective, extreme
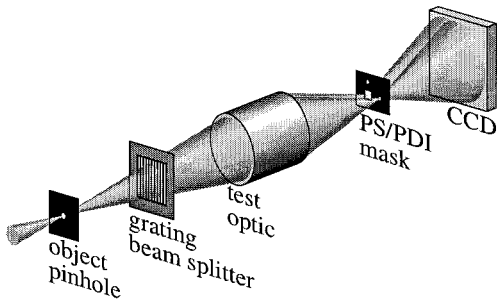
Fig. 1. Schematic representation of the PS/PDI. Pinhole diffraction in the object and the image planes produces spherical reference waves. A grating beam splitter creates multiple copies of the test beam, focused in the image plane. A mask containing a window and a very small pinhole transmits one test beam and spatially filters another to become the reference beam.

ultraviolet (EUV) optical systems that operate at a 13.4-nm wavelength[10,11] and in which the wave-front aberration tolerances are in the subnanometer regime.[12] Using reference pinholes on the order of 80-nm diameter, we have measured two- and four-mirror optical systems with NAs of as high as 0.1 and system wave-front aberration magnitudes on the order of 0.5-nm rms and below. Two-pinhole null tests have verified the high accuracy (0.004 waves, or 0.054-nm rms) that is attainable with the EUV PS/PDI.[13]

The mask window is usually designed to be centered about the test-beam focus when the reference beam is properly positioned on the reference pinhole. The window width in the direction of beam separation should be less than the beam-separation distance to minimize the undesirable overlap of the reference beam through the window. In the EUV application, with a typical beam separation of 5 μm (37 times λ/NA), the window widths are chosen to be less than the beam-separation distance.

The noise-suppression advantages of even smaller window sizes have been previously discussed.[14] An additional constraint may be imposed to achieve the complete separation of the orders in the Fourier domain of the recorded intensity image; here the window width must be limited to two thirds of the beam-separation distance.

Considering the small pinholes used in the measurement of high-resolution optical systems, alignment is the most challenging aspect of using the PS/PDI. This challenge is compounded in short-wavelength applications in which the interferometer exists inside a vacuum chamber and may be incompatible with other optical alignment strategies. Although the test beam is typically easy to align through the large image-plane window, the reference beam should be positioned onto the reference pinhole to within a fraction of the focal-spot diameter. The small size required of this pinhole attenuates the transmitted (diffracted) reference beam and narrows the capture range over which interference fringes are visible. During fine alignment, the intensity of the

test beam remains fixed, and one can judge optimum positioning by assessing the point of peak fringe contrast.

Until the reference pinhole is within the focus of the reference beam, only subtle clues are available to guide the alignment. This paper presents a convenient, effective, and easily implemented alignment method, called the Fourier-Transform Alignment Method (FTAM), based on the use of a real-time fast Fourier Transform (FFT) performed on the projected interference patterns recorded during alignment. Since this method is only used to facilitate alignment, it is unnecessary to seek high accuracy either in the calculation or in the description presented here. Emphasis is placed on qualitative description, and several simplifications are made to illustrate the behavior of this method in some common configurations.

As a further aid in the alignment of the PS/PDI, during alignment the FTAM is used to read encoded alignment marks and modifications to the window shapes; thus unambiguous placement of the beam(s) within an array of similar mask features is possible.[15]

2. Theory

This section describes the mathematical basis of the FTAM. Several examples are cited to illustrate the observable behavior of the system during alignment.

Owing to the detector's position in the far field of the image plane, the recorded images approximate the intensity, or square modulus, of the Fourier transform of the field transmitted through the PS/PDI image-plane mask. This complex transmitted field amplitude may be viewed as the product of the incident field from the test optic and the transmission function of the mask. With single-beam coherent illumination, in the absence of the grating beam splitter, the incident field is the point-spread function of the test optic. With the beam splitter installed, the incident field contains a series of similar image points. The transmission function of the mask is defined by the pattern of opaque and transparent regions and by the lateral position of the mask in the image plane.

In a single exposure, the detector measures the field intensity; phase information is temporarily lost. The Autocorrelation Theorem can be applied to the measured intensity to recover information about the field transmitted through the image plane at the back side of the mask. We label the complex transmitted image-plane field amplitude as $a(\boldsymbol{\rho})$, where $\boldsymbol{\rho}$ is a spatial coordinate vector in the image plane. In the Fraunhofer approximation[16] for the propagation of light from the image plane to the detector, the measured intensity is related to the Fourier transform of $a(\boldsymbol{\rho})$ evaluated at angular frequencies $\mathbf{f} = \mathbf{r}/\lambda z$, where $\mathbf{r}$ is a spatial coordinate in the detector plane, z is the distance to the detector plane, and λ is the wavelength. The detected field is $|A(\mathbf{r})|^2$, where A and a form a Fourier-transform pair. When $|A(\mathbf{r})|^2$ is
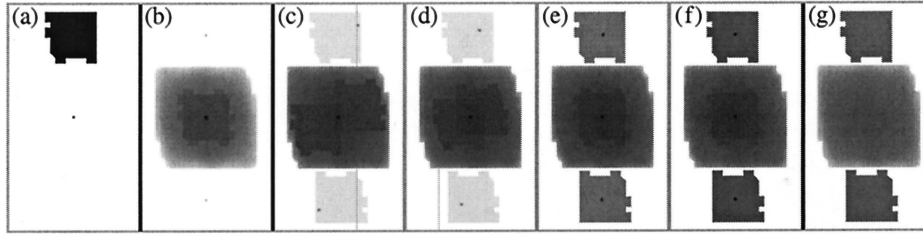
Fig. 2. PS/PDI mask (a) contains a large window for the transmission of the test beam and at least one small pinhole (shown at center)—black areas are transmissive, white are opaque. Features on the nominally square window aid in alignment. For several different configurations, (b)–(g) are simulations of the logarithmically scaled Fourier transform of the detected intensity, shown on inverted grayscale. (b) Test beam only, with the beam passing though the center of the window. (c)–(f) Intermediate steps in the alignment of the PS/PDI with the test beam passing through the window and the reference beam being aligned to pass through the pinhole. Optimal alignment is achieved (f) when the window is most clearly visible. (g) A single beam passes through the pinhole, with low-level, scattered light passing through the window.

known, the following relations in two dimensions hold

$$\mathcal{F}\{|A(\mathbf{r})|^2\} = \mathcal{F}\{A(\mathbf{r})A^*(\mathbf{r})\} \equiv a(\boldsymbol{\rho}) * a^*(-\boldsymbol{\rho}). \quad (1)$$

$\mathcal{F}$ signifies the Fourier transform, $*$ denotes the convolution operator, and superscript $*$ indicates the complex conjugate.

A. Alignment Procedure

The alignment procedure ends with the test beam passing through the window and the reference beam position optimized to pass through the reference pinhole with maximum intensity. There are several ways the alignment can proceed. In our experience, one successful method is to remove the grating beam splitter so there is only one focused beam in the image plane. Without much difficulty, this beam can be positioned to pass through the mask window.

If the one beam is to become the reference beam, either the mask or the beam position can be translated to optimize its position on the reference pinhole. At this point, the introduction of the beam splitter causes the test beam to pass through the center of the window, and the reference beam is aligned on the pinhole. Alternatively, if the first beam becomes the test beam, then when the beam splitter is introduced, fine alignment of the reference beam on the pinhole may be required.

Necessary prealigning of the beam splitter may include longitudinal position adjustment (to control beam-separation distance) and rotation angle (to control the beam-separation direction). The behavior of the FTAM during the intermediate alignment steps is described in the following sections.

B. Test Beam Alone

The field transmitted through the mask, $a(\boldsymbol{\rho})$, may be described as the product of the incident field and the mask transmission function, $m(\boldsymbol{\rho})$. The mask transmission function $m(\boldsymbol{\rho})$, which describes the mask pattern, includes the large window for the test beam and one or more reference pinholes close to the window. The incident field contains the focused beam, plus a lower level of scattered light or flare. For demonstration, we may approximate the focused beam as a

delta function and the light near the focus as having constant magnitude c of a smaller relative intensity. A more-detailed model of the image-plane field would accommodate the finite width of the focused beam and a nonuniform flare intensity, decaying away from the focus. These additional attributes could be considered during characterization of the performance of the FTAM under various conditions, but they do not enhance our understanding of how the FTAM works and are thus neglected from this heuristic model.

We approximate $a(\boldsymbol{\rho})$ as

$$a(\boldsymbol{\rho}) = [\delta(\boldsymbol{\rho}) + c]m(\boldsymbol{\rho} - \boldsymbol{\rho}_0), \quad (2)$$

where $\boldsymbol{\rho}_0$ is the lateral displacement of the mask relative to an arbitrary coordinate origin. When the test beam passes through the mask window unobstructed, $a(\boldsymbol{\rho})$ becomes

$$a(\boldsymbol{\rho}) = \delta(\boldsymbol{\rho}) + cm(\boldsymbol{\rho} - \boldsymbol{\rho}_0); \quad (3)$$

otherwise, when the mask blocks the focused test beam, $a(\boldsymbol{\rho})$ contains only $cm(\boldsymbol{\rho} - \boldsymbol{\rho}_0)$. Applying the approximation of Eq. (3) to Eq. (1), we have

$$\begin{aligned} \mathcal{F}\{|A(\mathbf{r})|^2\} &= [\delta(\boldsymbol{\rho}) + cm(\boldsymbol{\rho} - \boldsymbol{\rho}_0)] * [\delta^*(-\boldsymbol{\rho}) \\ &\quad + cm^*(\boldsymbol{\rho}_0 - \boldsymbol{\rho})] \\ &= \delta(\boldsymbol{\rho}) + [cm(\boldsymbol{\rho} - \boldsymbol{\rho}_0) + cm^*(\boldsymbol{\rho}_0 - \boldsymbol{\rho})] \\ &\quad + c^2 m(\boldsymbol{\rho}) * m^*(-\boldsymbol{\rho}). \quad (4) \end{aligned}$$

In this way, the Fourier transform of the measured intensity is separable into three components: a narrow peak at the origin, the low-level mask transmission function and its polar-symmetric complex conjugate folded about the point $\boldsymbol{\rho}_0$ and symmetric about the origin, and the autocorrelation of the mask transmission function, scaled by c^2. With magnitude proportional to c^2, the autocorrelation of m forms a low-level background signal about the central frequencies. The shape and extent of the autocorrelation of m depend on the shape of the window. In all cases, the autocorrelation reaches a maximum at the central frequency and decreases to zero at the position that corresponds to the full width of the window in each direction.

The configuration for the PS/PDI mask transmission pattern shown in Fig. 2(a) is depicted in Fig. 2(b). The magnitude of the Fourier transform of the detected intensity is shown with an inverted logarithmic scale (darker areas in the figure are actually brighter). Not included in Eq. (4) is the faint scattered light transmitted through the small pinholes and visible in Fig. 2(b).

Because the beam size in the mask plane varies with focus, the FTAM can also be used as a coarse test of the longitudinal alignment of the interferometer. When the mask is displaced from the image plane and the apparent size of the focal spot increases, the delta-function approximation of Eq. (3) must be replaced by a function having a finite width. In practice, this results in a noticeable blurring of the sharp window-edge features in the Fourier transform of the measured intensity. In the presence of moderate defocus, the longitudinal alignment can be adjusted while the sharpness of these features is assessed and optimized.

C. Test and Reference Beams

With a beam splitter used in the PS/PDI, the field from the test optic consists of a pair or a series of displaced copies of the point-spread function. The description of $a(\rho)$ in Eqs. (2) and (3) can be modified to include the other orders as follows. The spatial beam-separation vector between adjacent orders is $\mathbf{s}$. The series of displaced test-beam copies have peak amplitudes given by the coefficients $\{b_j\}$. We may write $a(\rho)$ as

$$a(\rho) = \left[\sum_j b_j \delta(\rho - j\mathbf{s}) + c \right] m(\rho - \rho_0). \quad (5)$$

If only one beam is transmitted through the mask window and all other beams are blocked, then the situation will be as in Eqs. (3) and (4), yet with an increased relative magnitude of c representing the combined flare from multiple beams.

When the PS/PDI is properly aligned for interferometry, the test beam passes through the mask window, and the reference beam is transmitted through the reference pinhole located at the position $\mathbf{s}$ from the origin. With the addition of the reference beam, interference fringes become visible in the detected intensity. This second beam in the image-plane field causes the Fourier transform of the detected intensity to take a different appearance.

Here, the reference beam in the image plane may be approximated as an additional displaced delta function of relative peak magnitude d. For example, when normalized to the intensity of the test beam, d may be equal to b_1/b_0. Spatial filtering by the reference pinhole reduces the reference beam magnitude to a new magnitude, d', upon transmission. Now the approximation for the transmitted field in the image plane is

$$a(\rho) = [\delta(\rho) + d\delta(\rho - \mathbf{s}) + c]m(\rho - \rho_0)$$
$$= \delta(\rho) + d'\delta(\rho - \mathbf{s}) + cm(\rho - \rho_0). \quad (6)$$

The three terms in Eq. (6) show how the mask pattern $m(\rho - \rho_0)$ transmits the incident field: the test beam is allowed to pass through the window unattenuated, $\delta(\rho)$; the displaced reference beam is reduced by pinhole spatial filtering, $d'\delta(\rho - \mathbf{s})$; and the background illumination fills the window, $cm(\rho - \rho_0)$.

Relative to Eq. (4) in the single-beam case, the autocorrelation of $a(\rho)$ now contains several additional terms.

$$\mathscr{F}\{|A(\mathbf{r})|^2\} = [\delta(\rho) + d'\delta(\rho - \mathbf{s}) + d'\delta^*(\mathbf{s} - \rho)]$$
$$+ [cm(\rho - \rho_0) + cm^*(\rho_0 - \rho) + cd'm(\rho - \rho_0 - \mathbf{s}) + cd'm^*(\rho_0 + \mathbf{s} - \rho)]$$
$$+ c^2 m(\rho) * m^*(-\rho). \quad (7)$$

There are now three narrow peaks in the Fourier transform: one at the origin and two displaced by the beam-separation vector(s) $\pm\mathbf{s}$, representing the reference beam and its complex conjugate. In addition to the two overlapped, polar-opposite mask patterns at the origin, which were present in Eq. (5), $m(\rho)$ and $m^*(-\rho)$ now appear at $\mathbf{s}$ and $-\mathbf{s}$, respectively.

Several intermediate steps in the alignment are shown in Figs. 2(c)–2(f). As the beam or the mask is translated laterally, the change in ρ_0 shifts only the positions of m and m^* in the spatial-frequency domain. Observation of this shifting is the basis of the FTAM. Observation of the motion of m and m^* in this way (i.e., in the Fourier transform of the detected intensity) allows the interferometer's operator to steer the test beam into the proper position in the mask window and the reference beam through the small pinhole. Owing to the speed of modern computers, this alignment can be performed with real-time feedback.

Notice in Figs. 2(c)–2(f) that as the reference beam is aligned to pass through the reference pinhole, the appearance of the windows becomes more pronounced. The visibility of the windows follows the increasing fringe contrast in the detected interference pattern from which the Fourier transform is calculated. The window visibility thus serves as a sensitive alignment indicator. An additional fine-alignment merit function based on fringe contrast is described in Section 4.

D. Reference Beam Alone

A final case for consideration is that of the isolated reference beam. In practice, this configuration can be used to judge the diffraction quality of a reference pinhole, separate from the interferometric measurement. It can also arise during alignment when the single beam is placed on the pinhole prior to the introduction of the beam splitter.

When the beam passes through the reference pinhole and only scattered light is transmitted through

the adjacent mask window, the situation can be approximated as

$$a(\mathbf{\rho}) = [d\delta(\mathbf{\rho}) + c]m(\mathbf{\rho} - \mathbf{s})$$
$$= d'\delta(\mathbf{\rho}) + cm(\mathbf{\rho} - \mathbf{s}). \quad (8)$$

By design, $\mathbf{s}$ is the distance between the reference pinhole and the center of the mask window. In this case, the detected intensity contains the broad pinhole diffraction pattern of the reference beam and some high-frequency components of the reference beam that pass through the window. The autocorrelation of $a(\mathbf{\rho})$ contains only three terms: a delta function at the zero-frequency position, two polar-symmetric displaced copies of the mask transmission function, and the low-level autocorrelation of the mask.

$$\mathscr{F}\{|A(\mathbf{\rho})|^2\} = d'^2\delta(\mathbf{\rho}) + [d'cm(\mathbf{\rho} - \mathbf{s})$$
$$+ d'cm^*(\mathbf{s} - \mathbf{\rho})] + c^2m(\mathbf{\rho}) * m^*(-\mathbf{\rho}). \quad (9)$$

This configuration, shown in Fig. 2(g), presents a way to investigate the quality of the reference beam since its broad diffraction pattern should be visible on the detector. As discussed in Section 3, it is also a good way to study *in situ* the characteristics of the test-beam window or the mask pattern. The single-beam configuration described here is equivalent to off-axis, Fourier-transform holography.[17]

E.   Measured Real Distances in the Fourier Domain

The capacity of this technique to reveal the features of the image-plane mask in the Fourier-domain analysis warrants a brief discussion of the relation between the spatial frequencies and the actual units of measurement. We derive a simple relation by analytically examining the interference pattern generated by two spherical waves originating from displaced point sources in the image plane.

When a given optical system with an NA NA is considered, the cone of light subtending the full angular range intersects the detector over an area that is n_{NA} pixels in diameter, where the full diameter of the detector contains $n_d (> n_{NA})$ pixels (n_d may be either the full size of the detector array or an appropriate subregion that is used in the Fourier-transform calculation). In this two-wave interference example, a point separation of $\lambda/(2\,NA)$ generates one wave of path-length difference, or one fringe across the full aperture of measurement (n_{NA} pixels). Therefore, a smaller separation of $(n_{NA}/n_d)\lambda/(2\,NA)$ generates one fringe across the n_d pixels of measurement and would appear in the Fourier domain as two symmetric delta-function peaks separated by a distance of two cycles. This result can be cast in a more convenient form. In the Fourier transform, the scaling of the pseudoimage is

$$\frac{\lambda[\mu m]}{4NA}\frac{n_{NA}}{n_d}\,[\mu m/cycle]. \quad (10)$$
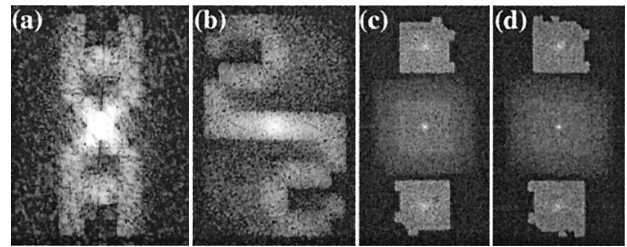

Fig. 3. Logarithmically scaled FFTs of experimental measurements of alignment marks demonstrate how these marks are read *in situ*. In (a) and (b), the single beam passes through the stenciled symbols in the image plane and is recorded in the far field by a detector. The Fourier transform of the recorded images is equivalent to the autocorrelation of the image-plane field and thus reveals the row and the column markers with a polar-symmetric reflected copy. The open areas are 1 μm wide. (c) and (d) Fourier transforms of interferograms recorded during PS/PDI measurement. A 3-bit binary code is patterned into the window edges to indicate the row and the column numbers within an array of similar marks. The windows are 3 μm wide; the alignment marks protrude by 1/3 μm from the square.

To demonstrate the scaling described by Eq. (10), consider the EUV PS/PDI operating at a 13.4-nm wavelength, measuring a test optic with NA 0.1. In this system, the full angular range of the pupil typically subtends 60% of the available detector width: the ratio n_{NA}/n_d equals 0.6. This scaling factor of 20 nm per cycle (or equivalently, 20 nm per pixel in the FFT pseudoimage) indicates a Fourier-domain separation of approximately 50 cycles per micrometer of real-space distance. The image-plane-mask windows, 3.0-μm wide, appear in the Fourier transform as approximately 150 cycles across. Features as small as two cycles wide, resolvable in the Fourier transform, correspond to mask features of 40 nm in length. In practice, however, the finite width of the reference beam's Fourier transform reduces this resolution slightly.

3.   Experimental Demonstration

As a demonstration of the FTAM, several characteristic images from the alignment of the EUV PS/PDI are shown in Fig. 3. The images are details of the central portion of the logarithmically scaled FFT magnitude of the detected signal. In Figs. 3(a) and 3(b), the optical system under test was a prototype molybdenum-silicon, multilayer-coated Schwarzschild objective operating with NA 0.08 at a 13.4-nm wavelength,[10] and the stenciled characters are pinhole-array row and column markers. Figures 3(c) and 3(d) are from the measurement of a four-mirror EUV optical system with NA 0.1.[18] Here, the PS/PDI-mask window is a 3-μm-wide square with binary row and column numbers encoded in the window border.[15] These images were generated when the system was in optimum alignment for interferometry.

In practice, the subtraction of signal-offset or background values can improve the appearance of the Fourier-transform image because spurious features

that appear as stripes in the central frequencies are eliminated. For alignment purposes, where a low-quality pseudoimage is acceptable, the presence of these spurious features is little more than a distraction.

As shown in Fig. 3, the ability of the FTAM to resolve fine features in the mask enables it to be used to investigate the field at the image plane, to probe other optical performance properties of a system under test (e.g., flare[19]), and to be used to identify patterned mask features designed as alignment aids.[15] Unambiguous stenciled alignment features are used to help an interferometer operator to align the test beam through known positions in an array of mask features.

The frame rate for this alignment technique, used in EUV interferometry, is determined by the exposure time, the readout rate of the CCD camera, and the scaling and display rate of the FFT image data. Using a 256×256 pixel image size, an 800-kHz readout rate, and a 0.1-s exposure time, we achieve alignment frame rates greater than 1 Hz.

Discussion: Since the FTAM relies on the intensity of the field in the halo surrounding the focused beam, it is important to understand the method's limitations in the case of low photon flux or with high-quality, low-flare optical systems. With the simple model of the focused beam, in which the image plane contains a delta-function peak surrounded by a uniform halo of constant field amplitude, the signal-to-noise (SN) requirements of the FTAM can be investigated. For this discussion, we assume that we are shot noise limited and not affected by detector saturation, or the detector's limited dynamic range.

Assume that in a single exposure, the beam illuminates M detector elements (pixels) to an average level of N photons per pixel within the measurement domain. This implies an energy of NM photons in the focused beam. Limited by shot noise, the measurement uncertainty is $N^{1/2}$ in each pixel. Correspondingly, the uncertainty in the elements of the discrete Fourier transform is $(NM)^{1/2}$. (Here in the convention employed for the forward Fourier transform a leading coefficient of unit magnitude is used: the dc, or zero-frequency, element of the Fourier transform is the unscaled discrete sum of the original function.)

The uniform halo has a known relative amplitude c, which is much less than unity. To understand the statistics of the image reconstruction, consider the coherent interaction of a single, arbitrary point in the halo with the central, focused peak. Light from these two sources forms a fringe pattern with contrast c. The discrete Fourier transform of that detected intensity pattern has a central peak of magnitude NM and two side peaks of magnitude $\frac{1}{2}MNc$. To be visible above the noise in the reconstruction, with an SN ratio (SNR) greater than or equal to one, requires $\frac{1}{2}NMc \geq (NM)^{1/2}$, hence,

$$NM \geq 4/c^2. \qquad (11)$$

Inequality (11) shows that the total number of detected photons required by the FTAM is inversely proportional to the square of the relative field amplitude in the halo or, equivalently, that the total number of detected photons is inversely proportional to the relative power density in the halo. There are many definitions of short-range flare; generally, the halo's relative power density is related to the flare by the inclusion of the area over which the halo is considered.

With a 256^2-element detector and a relative halo power density of 10^{-8}, the FTAM can be used with an average 6100 or more detected photons per pixel; a relative halo power density of 10^{-6} requires only 61 detected photons per pixel. A lithographic-quality EUV imaging system may have a 0.1-μm-diameter focal spot and a 4% flare in a 2-μm square surrounding the focus for a relative power density of approximately 10^{-4} in the halo. For such a system the FTAM can be used with modest exposure levels.

4. Alignment by Global Image Contrast

When the PS/PDI is nearly aligned and the interference of the test and reference beams is visible, fine adjustment of the components can be performed to optimize the appearance of the fringes across the measurement domain. The merit function of primary interest is the interference fringe contrast. Maximizing the fringe contrast directly improves the SNR in the measurement[20] and in most cases yields the highest reference-wave quality.

The calculations required by the FTAM lend themselves to the definition of a rapidly calculable global-fringe-contrast parameter, Γ, that can be used in alignment. Γ may be defined as the ratio of the power in the reference beam to the power of the test beam, as determined from the Fourier transform of the detected intensity. During alignment, it is not essential to calculate Γ with accuracy or high precision; as long as a consistent method of calculation is followed, the position of maximum contrast coincides with the position of maximum Γ. For the calculation speed to be increased, a subdomain of the interferogram (such as a central portion, a narrow ribbon of data, or even a single column through the center) may be used in the global-contrast calculations.

The *in situ* optimization of the global contrast with real-time feedback has become an important part in the final alignment steps of the PS/PDI. Small variations in the fringe contrast that are visually imperceptible to the operator are easily calculated and conveyed by a computer image-processing program.

5. Conclusion

The FTAM method has proved an invaluable tool in the rapid alignment of the EUV PS/PDI, and it may be applicable to various circumstances in which the alignment of components in the image plane of a coherently illuminated optical system is required. Using a relatively fast microprocessor, the logarithmically scaled magnitude of the FFT of the recorded intensity may be displayed alongside of the raw image in near real time.

This off-axis, Fourier transform holographic technique provides a powerful and convenient mode of alignment feedback for a system that is otherwise very challenging to align. In addition, this method provides a high-resolution pseudoimage of the image-plane field and optical components. Through off-axis, Fourier-transform holography, the ability to encode and read alignment marks in the pinhole mask further enhances the alignment technique and reduces potentially laborious position determination tasks.

A global-fringe-contrast parameter calculated from the Fourier-transform data may be used to judge the optimum fine alignment of the PS/PDI or any interferometer in which the Fourier-transform methods of single-interferogram analysis are applicable.

We note that it is conceptually possible to use *a priori* or measured phase information to supplement the recorded field intensity and further enhance this alignment technique. If the phase of the field incident on the CCD is known, beyond the measured intensity-only pattern, then the image-plane field can be reconstructed unambiguously, without the presence of additional and unwanted polar-symmetric pseudoimages. The incident-field magnitude is readily derived from the square root of the recorded intensity, and when a high-quality optic is under investigation, the field phase could be approximated as uniform.

References

1. W. P. Linnik, "A simple interferometer for the investigation of optical systems," Comptes Radnus de l'Académie des Sciences d'U.R.SS. **1,** 208 (1933).
2. R. N. Smartt and W. H. Steel, "Theory and application of point-diffraction interferometers (telescope testing)," Jpn. J. Appl. Phys. **14** (Suppl. 14-1), 351–356 (1975).
3. R. J. Speer, M. Chrisp, D. Turner, S. Mrowka, and K. Tregidgo, "Grazing incidence interferometry: the use of the Linnik interferometer for testing image-forming reflection systems," Appl. Opt. **18,** 2003–2012 (1979).
4. G. E. Sommargren, "Diffraction methods raise interferometer accuracy," Laser Focus World **32,** 61–71 (1996).
5. H. J. Jeong and D. A. Markle, "Point diffraction interferometer and pin mirror for use therewith," U.S. patent 5,822,066 (13 October 1998).
6. O. Y. Kwon, "Multichannel phase-shifted interferometer," Opt. Lett. **9,** 59–61 (1984).
7. C. R. Mercer and K. Creath, "Liquid-crystal point-diffraction interferometer," Opt. Lett. **19,** 916–918 (1994).
8. H. Medecki, E. Tejnil, K. A. Goldberg, and J. Bokor, "Phase-shifting point diffraction interferometer," Opt. Lett. **21,** 1526–1528 (1996).
9. P. P. Naulleau, K. A. Goldberg, S. H. Lee, C. Chang, D. Attwood, and J. Bokor, "Extreme-ultraviolet phase-shifting point-diffraction interferometer: a wave-front metrology tool with subangstrom reference-wave accuracy," Appl. Opt. **38,** 7252–7263 (1999).
10. E. Tejnil, K. A. Goldberg, S. H. Lee, H. Medecki, P. J. Batson, P. E. Denham, A. A. MacDowell, J. Bokor, and D. T. Attwood, "At-wavelength interferometry for EUV lithography," J. Vac. Sci. Technol. B **15,** 2455–2461 (1997).
11. K. A. Goldberg, P. Naulleau, P. Batson, P. Denham, H. Chapman, and J. Bokor, "Extreme ultraviolet alignment and testing of a four mirror aspheric extreme ultraviolet optical system," J. Vac. Sci. Technol. B **18,** 2911–2915 (2000).
12. D. M. Williamson, "The elusive diffraction limit," in *Extreme Ultraviolet Lithography*, Vol. 23 of OSA Proceedings Series, D. T. Attwood and F. Zernike, eds. (Optical Society of America, Washington, D.C., 1994), pp. 68–76.
13. P. Naulleau, K. A. Goldberg, S. Lee, C. Chang, C. Bresloff, P. Batson, D. Attwood, and J. Bokor, "Characterization of the accuracy of EUV phase-shifting point diffraction interferometry," in *Emerging Lithographic Technologies II*, Y. Vladimirski, ed., Proc. SPIE **3331,** 114–123 (1998).
14. P. P. Naulleau and K. A. Goldberg, "A dual-domain point diffraction interferometer," Appl. Opt. **38,** 3523–3533 (1999).
15. K. A. Goldberg and P. P. Naulleau, "*In situ* alignment system for phase-shifting point-diffraction interferometry," U.S. patent 6,118,535 (12 September 2000).
16. J. W. Goodman, *Introduction to Fourier Optics*, 2nd ed. (McGraw-Hill, New York, 1988).
17. E. N. Leith and J. Upatnieks, "Reconstructed wavefronts and communication theory," J. Opt. Soc. Am. **52,** 1123–1130 (1962).
18. K. A. Goldberg, P. Naulleau, P. J. Batson, P. Denham, E. H. Anderson, J. Bokor, and H. N. Chapman, "EUV interferometry of a four-mirror ring-field EUV optical system," in *Emerging Lithographic Technologies*, E. A. Dobisz, ed., Proc. SPIE **3997,** 867–873 (2000).
19. P. Naulleau, K. Goldberg, E. Gullikson, and J. Bokor, "At-wavelength, system-level flare characterization of EUV optical systems," Appl. Opt. **39,** 2941–2947 (2000).
20. K. A. Goldberg, "EUV Interferometry," Ph.D. dissertation (University of California, Berkeley, 1997).